RESEARCH ARTICLE

Key Points:
- Mountain waves penetrate the mesosphere under suitable propagation conditions
- Small-scale gravity waves can attain very large momentum fluxes
- Occurrence of peak momentum fluxes is often dictated by multiscale environments

Momentum flux estimates accompanying multiscale gravity waves over Mount Cook, New Zealand, on 13 July 2014 during the DEEPWAVE campaign

Katrina Bossert[1,2], David C. Fritts[1], Pierre-Dominique Pautet[3], Bifford P. Williams[1], Michael J. Taylor[3], Bernd Kaifler[4], Andreas Dörnbrack[4], Iain M. Reid[5,6], Damian J. Murphy[7], Andrew J. Spargo[6], and Andrew D. MacKinnon[6]

[1]GATS Inc., Boulder, Colorado, USA, [2]Aerospace Engineering Science, University of Colorado Boulder, Boulder, Colorado, USA, [3]Center for Atmospheric and Space Sciences, Utah State University, Logan, Utah, USA, [4]Institute of Atmospheric Physics, German Aerospace Center, Oberpfaffenhofen, Germany, [5]School of Physical Sciences, University of Adelaide, Adelaide, South Australia, Australia, [6]ATRAD Pty Ltd., Thebarton, South Australia, Australia, [7]Australian Antarctic Division, Department of the Environment, Kingston, Tasmania, Australia

Abstract Observations performed with a Rayleigh lidar and an Advanced Mesosphere Temperature Mapper aboard the National Science Foundation/National Center for Atmospheric Research Gulfstream V research aircraft on 13 July 2014 during the Deep Propagating Gravity Wave Experiment (DEEPWAVE) measurement program revealed a large-amplitude, multiscale gravity wave (GW) environment extending from ~20 to 90 km on flight tracks over Mount Cook, New Zealand. Data from four successive flight tracks are employed here to assess the characteristics and variability of the larger- and smaller-scale GWs, including their spatial scales, amplitudes, phase speeds, and momentum fluxes. On each flight, a large-scale mountain wave (MW) having a horizontal wavelength ~200–300 km was observed. Smaller-scale GWs over the island appeared to correlate within the warmer phase of this large-scale MW. This analysis reveals that momentum fluxes accompanying small-scale MWs and propagating GWs significantly exceed those of the large-scale MW and the mean values typical for these altitudes, with maxima for the various small-scale events in the range ~20–105 $m^2 s^{-2}$.

1. Introduction

Gravity wave (GW) momentum transport and deposition throughout the atmosphere have significant impacts on Earth's weather and climate. Momentum deposition causes drag on mean and larger-scale winds, resulting in reversals of the mesospheric jets, an induced residual circulation that impacts mean temperatures from the lower altitudes into the mesosphere and lower thermosphere (MLT), and modulations of larger-scale motions and their mapping to higher altitudes [e.g., *Holton*, 1982, 1984; *Garcia and Solomon*, 1985; *Haynes et al.*, 1991; *Smith*, 2003; *Fritts and Alexander*, 2003; *Kim et al.*, 2003; *Lieberman et al.*, 2010, 2013]. Many studies suggest that GWs having smaller horizontal wavelengths and higher intrinsic frequencies contribute significantly to the total momentum budget [e.g., *Vincent and Reid*, 1983; *Fritts and Vincent*, 1987]. In some cases, small-scale GW momentum fluxes (MFs) are tied to specific sources such as orography and convection [e.g., *Nastrom and Fritts*, 1992; *Pfister et al.*, 1993]. In other cases, strong localized GW packets exhibit no obvious sources and more likely achieve large amplitudes and MFs due to filtering by the larger-scale environments [e.g., *Hertzog et al.*, 2012; *Fritts et al.*, 2002, 2014]. Some modeling studies show that smaller-scale GWs may be significantly influenced by multiscale GW environments [*Eckermann*, 1997]. Despite many studies and valuable insights, much remains to be learned about the multiscale interactions that influence small-scale GW behavior and the character and statistics of small-scale GW contributions to total MFs throughout the atmosphere.

Many studies using individual instruments or instrument suites have contributed to our understanding of GWs at larger and smaller scales. Ground-based instruments such as lidars, airglow imagers, and radars have been used to characterize GW activity [e.g., *Fritts*, 1984, and references therein; *Wilson et al.*, 1991; *Collins et al.*, 1996; *Taylor et al.*, 1997; *Yue et al.*, 2009]. Lidars allow for a vertical and temporal characterization of GWs and profiles of buoyancy frequency and/or background winds that define the GW propagation environment. Airglow imagers provide valuable information on GW horizontal scales, orientations, and propagation directions that are challenging to infer from lidars and radars alone. The more recent Advanced Mesosphere

Temperature Mappers (AMTMs) also provide temperature images at the OH layer [*Pautet et al.*, 2014], which prove especially valuable in quantifying small-scale GW amplitudes and MFs [e.g., *Fritts et al.*, 2014]. Indeed, various combinations of these instruments have contributed greatly to a broader understanding of GWs over many years [e.g., *Collins and Smith*, 2004; *Williams et al.*, 2006; *Namboothiri et al.*, 1996; *Hecht et al.*, 1997; *Nielsen et al.*, 2012; *Bossert et al.*, 2014; *Cai et al.*, 2014; *Yuan et al.*, 2014; *Ejiri et al.*, 2009; *Simkhada et al.*, 2009] because such combinations of instruments allow for a more complete quantification of GW environments and parameters.

Measurements from various instruments allow for the quantification of mean and variable GW momentum flux within the MLT. Multiple radars from equatorial to polar latitudes have revealed typical mean zonal momentum flux magnitudes of $<u'w'>$ ~1–20 $m^2 s^{-2}$ in the MLT that are anticorrelated with zonal mean winds and with lower (higher) values at lower (higher) altitudes and latitudes [*Vincent and Reid*, 1983; *Fritts and Vincent*, 1987; *Reid et al.*, 1988; *Tsuda et al.*, 1990; *Wang and Fritts*, 1990; *Hitchman et al.*, 1992; *Fritts et al.*, 2010, 2012; *Murphy and Vincent*, 1993; *Nakamura et al.*, 1993]. Global MF averages from satellites have provided previous estimates ranging from ~1 to 8 $m^2 s^{-2}$ in the MLT [*Ern et al.*, 2011]. Local estimates for short-term (~1–6 h) averages using radars are often ~30–60 $m^2 s^{-2}$ or larger, while local estimates employing airglow observations suggest systematic geographic conditions and occasional, very strong events having $<u'w'>$ magnitudes as large as ~900 $m^2 s^{-2}$ [*Fritts et al.*, 2014; *Espy et al.*, 2004]. Finally, satellite measurements have allowed for calculations of the residual-mean circulation and provided estimates of total wave drag (assumed to be due primarily to GWs in the mesosphere) that are similar in form to but somewhat smaller in magnitude than radar measurements at corresponding latitudes and altitudes [*Lieberman et al.*, 2000].

The Deep Propagating Gravity Wave Experiment (DEEPWAVE) research program was conceived to take advantage of the synergism between multiple instruments and performed measurements addressing GW responses to multiple sources throughout a large and active source region. For these purposes, DEEPWAVE employed two new airborne lidars and an AMTM developed specifically for the National Science Foundation/National Center for Atmospheric Research (NSF/NCAR) Gulfstream V (GV) research aircraft. These measurement capabilities were augmented by a second aircraft, the German DLR Falcon having in situ instruments and a downward viewing aerosol Doppler lidar and extensive ground-based measurements extending from the surface to ~100 km on the New Zealand South Island and Tasmania. An overview of the DEEPWAVE program [*Fritts et al.*, 2015] describes the program motivations, measurement and modeling capabilities, performance, and initial results. DEEPWAVE was performed on and over South Island, Tasmania, and the surrounding Southern Ocean and Tasman Sea during June and July 2014, with aircraft operations and program logistics based in Christchurch.

Research reported here addresses GW dynamics observed by the GV Rayleigh lidar, AMTM, and two IR "wing" cameras at altitudes from ~20 to 90 km on Research Flight 22 (RF22) performed on 13 July, one of the 26 GV research flights performed throughout DEEPWAVE. The DEEPWAVE instrumentation and data are described in section 2. Sections 3 and 4 describe the estimates of GW parameters and momentum fluxes. A discussion of the results and our conclusions are provided in sections 5 and 6.

2. Research Data and Instrumentation

DEEPWAVE data employed for this study were collected with the new GV Rayleigh lidar, AMTM, and wing cameras viewing the OH layer to either side of the GV in order to extend the cross-track imaging to ~900 km. A brief description of each measurement capability and data analysis is provided below.

2.1. GV Advanced Mesosphere Temperature Mapper

The GV AMTM is a newly developed IR imager measuring selective lines of the OH (3,1) emission. This bright emission originates from a ~8 km full width at half maximum (FWHM) layer located at ~87 km in altitude [*Baker and Stair*, 1988; *She and Lowe*, 1998] and is widely used as a tracer of the dynamical processes propagating through the upper atmosphere. The AMTM comprises a 320×256 pixel IR sensor, a large-aperture telecentric lens system, and a computer-controlled filter wheel to sequentially measure the brightness of the $P_1(2)$ and $P_1(4)$ lines of the OH (3,1) band, as well as the atmospheric background. Combining these three emissions, it is possible to calculate the OH (3,1) rotational temperature for each pixel of an image and "map"

the mesospheric temperature over a ~120 × 80 km area [*Pautet et al.*, 2014]. During the DEEPWAVE flights, the exposure time for each filter was 4 s, providing a temperature measurement every ~16 s, with a typical error of ±2 K for each individual pixel. In the months preceding the campaign, cross calibration was performed by operating the AMTM alongside the well-proven Utah State University Na lidar. The two instruments were in good agreement on individual nights as well as on an average basis. The accuracy relative to the lidar measurements at 87 km was <1 K. In addition to the AMTM, two low-elevation (25° above the horizon) IR imagers were operated on each side of the plane. They only measured the OH emission brightness, but their large field of view (~40 × 30°) allowed to laterally extend the region of the MLT observed from the aircraft and to investigate the large-scale gravity waves covering its surroundings.

2.2. GV Rayleigh Lidar

The Rayleigh lidar is a new facility instrument built at GATs Inc. for the NSF/NCAR Gulfstream V. This lidar and the GV sodium lidar are contained in two standard GV instrument racks. The laser is a diode-pumped Nd:YLF Photonics DS20-351 generating 5 W at a 351 nm wavelength and a 1 kHz pulse repetition rate. The beam is expanded to 20 mm diameter and 0.4 mrad divergence, so that it is eye safe for 0.25 s exposures when it exits the laser windows on the top of the aircraft. The return signal is received using a 0.3 m diameter f/4 Newtonian telescope. The fiber-coupled detector is a 50% quantum efficiency, low-noise photomultiplier tube with a 0.5 nm FWHM interference filter. The returned signal profiles are recorded at 1 s temporal and 37.5 m altitude resolution.

Following the normal Rayleigh procedure, an atmospheric density profile is calculated from the lidar signal profile taking into account the geometric factors. The density is integrated down from a top starting temperature to obtain a temperature profile. For the start temperature, we used the European Centre for Medium-Range Weather Forecasts (ECMWF) model temperature at 71 km interpolated to the aircraft time and position. This calculation assumes that there is no aerosol scatter. Temperature results are shown from 20 to 60 km. At 40 km altitude, the temperature error is ~2 K in a 30 s, 3 km integration.

2.3. GV Sodium Lidar

The sodium lidar is a high spectral resolution system that shares the same racks, telescope, and receiver electronics as the Rayleigh system. The transmitter is a narrowband Toptica continuous wave laser composed of a 18 W Raman fiber amplifier doubled to produce 10 W of 589 nm light with a 10 MHz line width. The laser output light is locked to the D2a feature in the sodium Doppler-free saturation spectrum. We use an acousto-optic amplitude modulator to produce 20 μs square pulses repeating at 1 kHz. This modulator produces a small 80 MHz frequency shift, which we account for in the analysis. This pulsed beam has a 150 km total range and 3 km range resolution.

The receiver is fiber coupled to the telescope. We use a 75% transmission 1 nm bandwidth interference filter and a 40% quantum efficiency photomultiplier tube. This beam is synchronized with the Rayleigh beam to avoid cross talk, and the data are recorded on the same counter board oversampled at 1 s and 37.5 m resolutions. For postprocessing, the counts are averaged in bins of 1 km and 3.2 min (~45 km spatially) and Rayleigh normalized at altitudes from 30 to 35 km using Mass Spectrometer Incoherent Scatter (MSIS). The mixing ratios are calculated from sodium densities and relative background atmospheric conditions based on a scale height calculated from the AMTM temperature and MSIS densities at 87 km.

2.4. Lauder Rayleigh Lidar

The German Aerospace Center (DLR) Rayleigh lidar at Lauder (45.0°S, 169.7°E) is a mobile mesospheric lidar system contained in an 8 foot container. The transmitter comprises a diode-pumped Nd:YAG laser generating 12 W at 532 nm wavelength and 100 Hz pulse repetition rate. Backscattered light is collected using a fiber-coupled 25 inch diameter telescope mirror with a field of view (FOV) of 0.24 mrad. In the receiver the light is distributed between three detectors, a 608 nm Raman channel and low and high rate 532 nm channels. The timing of detected photons is recorded at 2 ns resolution. The temperature is initialized at 95 km. For the nightly average, the count profiles are vertically averaged over a 900 m resolution.

2.5. Kingston Meteor Detection Radar

An ATRAD meteor detection wind radar, capable of measuring wind speeds between heights of 70 and 110 km, operated at Kingston, Tasmania (43.0°S, 147.3°E), from 10 June 2014 through the DEEPWAVE

measurement program. The radar consisted of a high-power pair of crossed folded dipole antennas for circularly polarized all-sky transmission at the radar frequency of 55.0 MHz and a Mills cross array of five crossed Yagi receiving antennas. Transmitted power was 40 kW peak. Winds were derived at equally spaced heights by least squares fitting a nondivergent wind field to 1 h windows of radial velocity determinations. A general system description of this type of meteor radar is given by *Holdsworth et al.* [2004].

3. Determination of GW Parameters

The observed GWs were characterized using the methods and equations from *Fritts et al.* [2014] and *Fritts and Alexander* [2003], an overview of which is provided here. The GW perturbations are assumed to have the approximate forms given by

$$\widetilde{u}, \widetilde{w}, \widetilde{T}, \widetilde{p}, \widetilde{\rho} \sim u', w', \frac{T'}{\overline{T}}, \frac{p'}{\overline{p}}, \frac{\rho'}{\overline{\rho}} \left(\exp\left[i(kx + mz - \omega t) + \frac{z}{2H}\right] \right) \tag{1}$$

Where u', w', T', p', and ρ' are horizontal and vertical velocity, temperature, pressure, and density perturbations; $\overline{T}$ is the mean temperature; $\overline{\rho}$ is the mean density; $\omega = kc$ is the GW frequency; and H is the scale height. The buoyancy frequency squared is given by

$$N^2 = \frac{g}{\overline{T}} \left[\frac{d\overline{T}}{dz} + \frac{9.5K}{km} \right] \tag{2}$$

From the polarization relations in *Fritts and Alexander* [2003], the momentum flux (MF) averaged over a wavelength of a GW can be obtained as follows:

$$MF = <u'w'> = \frac{1}{2} u'^2 \left(\frac{k}{m}\right) = \frac{1}{2} \left(\frac{T'}{\overline{T}} \frac{g}{N}\right)^2 \left(\frac{k}{m}\right) \tag{3}$$

The above equation calculates the vertical flux of horizontal momentum. Here $k = 2\pi/\lambda_h$ is the horizontal wave number, $m = 2\pi/\lambda_z$ is the vertical wave number, and λ_h and λ_z are the horizontal and vertical wavelengths, respectively. Equation (3) gives a low-end estimate for MF, as it uses raw temperatures and does not account for phase averaging over the hydroxyl layer. For an ideal GW propagating through the hydroxyl layer, the temperature perturbation, T', can be corrected by dividing by a correction factor, C_F, as $T'\text{corr} = T'/C_F$. The correction factor, C_F, for this ideal case is given in equation (4).

$$C_F = \frac{<T'>}{T'(z_o)} = \exp\left[\frac{-\pi^2 z_{FWHM}^2}{4\ln(2)\lambda_z^2}\right] = \exp\left[-3.56\frac{z_{FWHM}^2}{\lambda_z^2}\right] \tag{4}$$

The quantity $<T'>$ in equation (4) is the temperature perturbation measured by the AMTM, which is smaller than the true T' amplitude due to phase averaging over the OH layer. The Sounding of the Atmosphere using Broadband Emission Radiometry (SABER) instrument on the TIMED satellite measured the OH profile on an overpass near South Island on 13 July that indicated an OH layer height of ~87 km and an OH layer FWHM of ~7 km. With the GW λ_h and k from the AMTM, m can either be derived from lidar data (with sufficient resolution and altitude coverage) or determined from the dispersion relation

$$m^2 = \frac{N^2}{(c - u)^2} - \frac{1}{4H^2} - k^2 \tag{5}$$

Here c is the observed phase speed of the GW and u is the local background wind. Using lidar data and the AMTM, the MF can be calculated for observed GWs where the background conditions can be suitably approximated. This method is used to provide MF estimates for individual GW packets in the following section.

4. Momentum Flux Estimates

4.1. Observed GW Fields

The four cross-island GV flight segments on RF22 occurred between 6:15 and 9:10 UT (18:15–21:10 local time) and were each ~530 km in length. Each flight segment was sufficiently long to identify approximately two wavelengths of a stationary, large-scale MW seen in both the Rayleigh lidar temperatures from 20 to 60 km in altitude and in the AMTM and IR camera OH brightness at the OH layer altitude (~87 km). The side-viewing OH
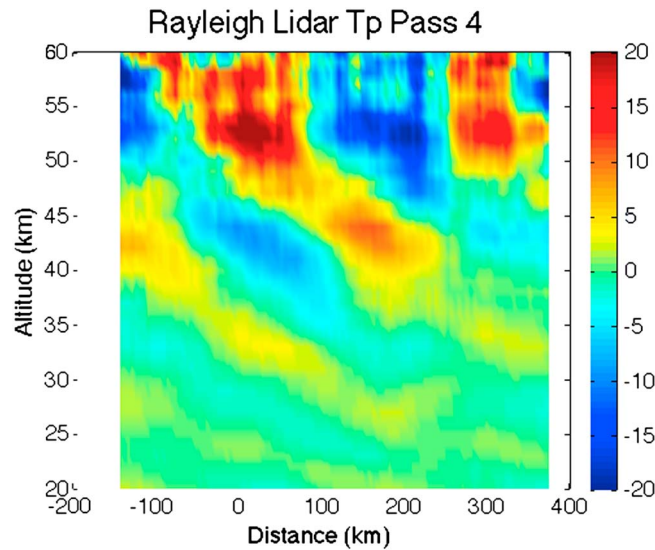
Figure 1. Rayleigh lidar temperature perturbations from the fourth pass show a vertical wavelength of ~20 km.

brightness images confirm that the phase fronts of the large-scale MW were indeed stationary along each pass. The slightly extended (east-west) imaging data suggest a MW λ_h varying from ~200 km at the eastern side of each flight segment to ~300 km at the western side, with a mean of $\lambda_h \sim 240$ km. Thus, we will assume the mean value for our analysis here.

The 240 km MW observed by the Rayleigh lidar is shown as a $T'(x,z)$ zonal-vertical cross section for flight segment 4 in Figure 1. $T'(x,z)$ was obtained by subtracting an averaged background temperature for the segment. This MW exhibits a pronounced increase in both its amplitude and its vertical wavelength with increasing altitude. T' varies from a few kelvins at the lower altitudes to ~15 K or larger at ~52 km and above. We expect amplitude growth with altitude for conservative GW propagation. At lower altitudes between ~20 and 55 km, the growth with altitude is a factor of ~8–10, which is expected for a GW with a mean scale height of $H \sim 6$–7 km that is growing in amplitude without significant dissipation. Likewise, λ_z increases with altitude from ~10 km or less below ~30 km in altitude to ~20–30 km at the higher altitudes. The changing vertical wavelength of the $\lambda_h \sim 240$ km MW is consistent with the increase in zonal wind predicted by the ECMWF model. For reference, Figure 2 shows the averaged zonal winds from ECMWF for the duration of the flight and the minimum and maximum values throughout the ECMWF domain. The increasing ECMWF zonal winds correlate with the increasing vertical wavelength observed in the Rayleigh lidar above 20 km. Additionally, we see that there was some modulation in the vertical phase structure of the $\lambda_h \sim 240$ km MW at intermediate and higher altitudes. This could have resulted from a superposition of MWs having other scales or phase slopes, or other propagating GWs, but uncertainties grow exponentially with altitude, so it is not possible to be confident of estimates based on Rayleigh lidar measurements approaching 60 km.
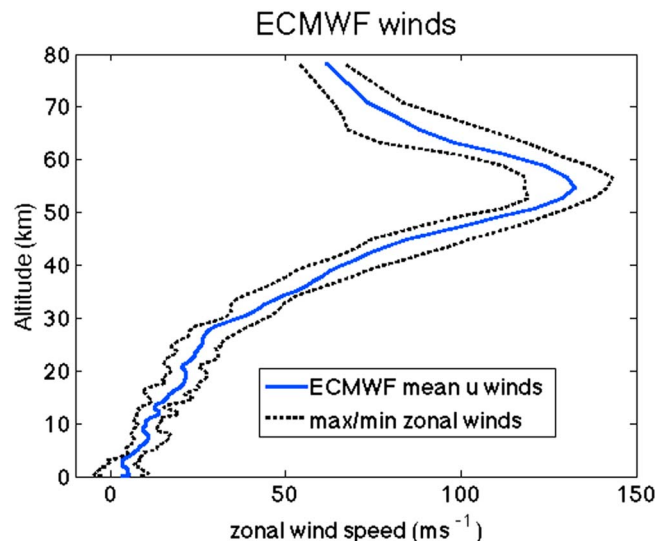

Figure 2. ECMWF winds averaged over the duration of the flight with the maximum and minimum winds included for reference.

As a guide for our inferences of MW and other GW structures seen in the AMTM data at higher altitudes, we note that a decreasing mean temperature above the stratopause would cause a smaller N and an increase in λ_z with altitude, whereas an expected reduction of the zonal wind would cause a decrease in λ_z with altitude.

DEEPWAVE forecasts by the European Center for Medium-Range Weather Forecasts (ECMWF) provided for flight planning and analysis purposes for RF22 (not shown) agree reasonably well with the T' fields obtained with the Rayleigh lidar and suggest refraction to somewhat smaller $\lambda_z \sim 20$ km above 60 km altitudes, apparently in response to the larger influences of weakening zonal winds above. Additionally,
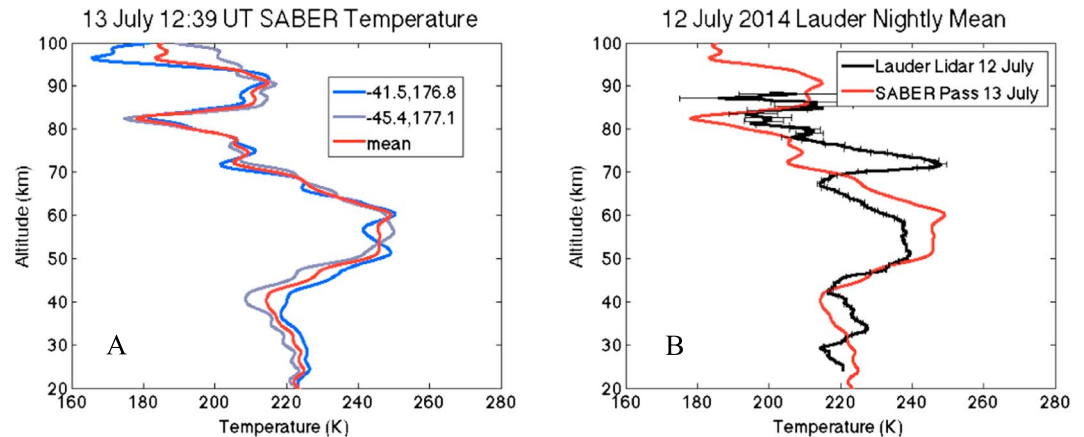
Figure 3. (a) Saber temperatures from two passes on 13 July 2014 at 12:38:21 and 12:39:31 and the averaged temperature between these passes. (b) The nightly average from the Lauder Rayleigh lidar on 12 July 2014 plotted with the averaged SABER temperature from Figure 3a.

ECMWF predicts that the particular conditions allowing the large-scale ~240 km MW to propagate to high altitudes existed for approximately 2 days, beginning on 12 July. While data from the nearby Lauder station were unavailable during the RF22 flight, Rayleigh lidar data were available from Lauder for 12 July. We believe that these data provide a good estimate of local temperatures between 60 and 85 km during RF22, given that ECMWF predicts that this event extends over these 2 days. Furthermore, SABER temperatures [*Remsberg et al.*, 2008] are available nearby at ~12:30 UT on 13 July, just a few hours after the RF22 flight. These temperatures also provide an estimate of large-scale temperature environment within which these DEEPWAVE measurements were performed. Differences of the Lauder lidar profiles from the SABER profiles then provide indications of local variations that may be largely due to MWs. Figure 3a shows the individual mean temperature profiles for the two SABER profiles. Figure 3b shows the nightly average of the Lauder Rayleigh lidar temperatures with the mean SABER temperatures. Both the lidar and SABER show a strong negative gradient in temperature between ~70 and 80 km. However, this differs in altitude between the two measurements. The lidar shows this low-stability layer to extend from ~70 to 77 km, and SABER shows it to extend from ~77 to 82 km. Both the lidar and SABER show a positive temperature gradient from ~80 to 90 km. The difference between these measurements likely indicates local influences of the MW in the lidar data, which likely makes little contribution to the limb-averaged SABER profiles. The weakly stable layer in the lidar profile between ~70 and 80 km suggests a potential for sustained MW breaking at these altitudes during these times.
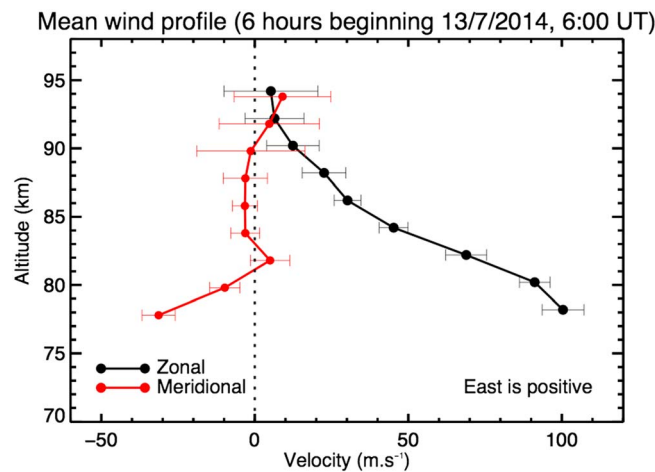

Figure 4. Kingston meteor radar wind 6 h mean starting at 6 UT on 13 July 2014 shows winds of 45 m s^{-1} toward the east at 84 km and 25 m s^{-1} toward the east at 87 km.

A rough prediction of winds for the time period of RF22 can be obtained from the Kingston radar over Tasmania. While these radar winds are ~2000 km away from the measurements over New Zealand, they provide a reasonable estimate of the mean winds and tidal influences at the altitudes, latitude, and local time of our measurement. A 6 h total wind starting at 6:00 UT is shown in Figure 4. These measurements suggest a mean wind of about ~25 m s^{-1} toward the east near 87 km at the peak of the hydroxyl layer.

Turning to the hydroxyl layer, Figure 5 shows for reference the GV AMTM and wing camera horizontal map of OH airglow brightness along and across the
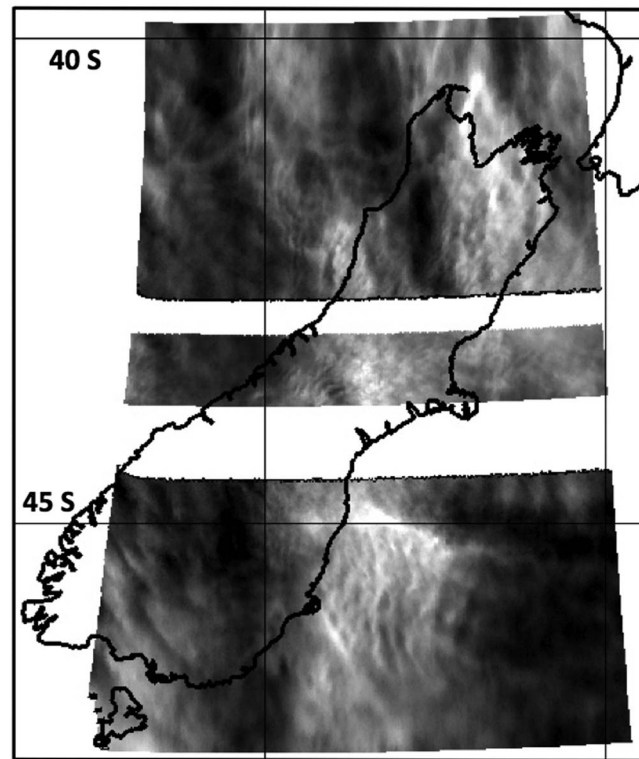
Figure 5. Imager intensities from the fourth pass of RF22 using the AMTM and side-viewing IR cameras. These intensities show the ~240 km MW positioned over the South Island of New Zealand and spanning ~900 km meridionally.

flight track for flight segment 4. The horizontal dimensions of this field are ~600 km east-west and ~900 km north-south. Seen clearly are three large-scale bright regions oriented nearly north-south, with the stronger central feature crossing the center of South Island.

Sodium mixing ratios computed along this flight provide additional insights into the evolution of the ~240 km MW in altitude and time. Figure 6 shows the sodium mixing ratio contours for each pass, for which a horizontal averaging of ~45 km has been employed. While these contours do not have the resolution to show smaller-scale GW activity, they clearly demonstrate the ~240 km MW observed on each pass. The contours show that the large-scale MW has an appreciable amplitude up to ~80 km but has largely dissipated by ~87 km. The inferred decrease of the ~240 km MW amplitude over this altitude interval and the near-vertical Na mixing ratio contours suggesting possible MW breaking and overturning appear to be consistent with the observation by both the Lauder lidar and SABER of a layer of low stability located near ~70–80 km and the observation by the Kingston radar of a critical level for MWs near 90 km altitude. Given these sodium mixing ratios, combined with the environments predicted by the Lauder Rayleigh lidar and the Kingston radar, the OH airglow measurements are likely responding to the ~240 km MW perturbations below the OH layer maximum where the amplitude and vertical wavelength are largest as opposed to the regions above 85 km where the ~240 km MW has largely dissipated.

Shown in Figure 7 are the corresponding GV AMTM along-track temperature fields for all four flight segments. These along-track field maps, also called keograms, were created using successive zenith cross sections from the AMTM that have been stitched together to create a spatial view of the temperatures along the flight path. Comparing the brightness and temperature fields for flight segment 4, we see that the regions of warmest temperatures correspond closely to the regions of maximum brightness. The particular features of greatest interest in this paper also occur in the brightest, and apparently warmest, and largest amplitude, phase of the ~240 km MW.

The along-track AMTM temperatures reveal the presence of smaller-scale GWs with $\lambda_h \sim 25$–28 km primarily within the bright and warm phases of the ~240 km MW on each flight segment. For our discussion below, we will employ the reference frame of the ~240 km MW, defining positive zonal velocities to be in the propagation direction of this MW (thus positive toward the west). We assume that the ~240 km MW is propagating approximately zonally, upward, and to the west. The following analysis yields approximate values for MF, allowing us to qualitatively estimate the MF influences of the observed GWs along this flight. We note that the corresponding MF calculations are likely an underestimate of the actual MF values. However, these values are nonetheless important in highlighting the influences of these observed GWs as they show the tendency for large magnitudes in such environments even for these underestimates. Where appropriate, upper bounds on MF are estimated or ranges of MF estimates are given based on uncertainties in observed GW amplitudes and other derived quantities.

4.2. Background Environment

The background temperature profile was estimated given the information from the Lauder Rayleigh lidar and SABER temperature measurements. Above the nearly adiabatic layer from ~70 to 80 km, we assume a slightly
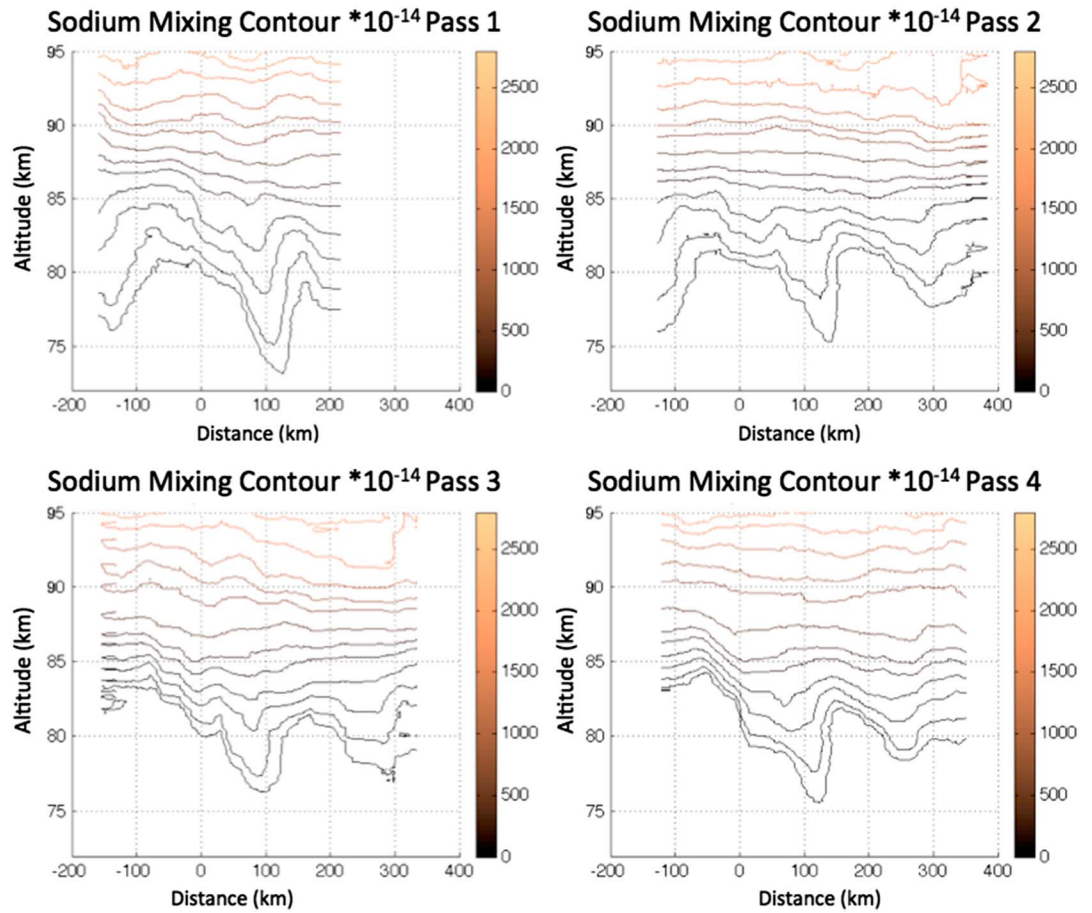
Figure 6. Sodium mixing ratios from the GV sodium lidar for the four RF22 flight segments clearly show the ~240 km MW below 85 km and strong dissipation of this MW above 85 km.

positive temperature gradient above 80 km. The nightly average from the AMTM was found to be 212 K, and that from the Lauder Rayleigh lidar at ~80 km was ~195 K. SABER provides a temperature of 194 K at 80 km and 211 K at 87 km. While both of these measurements include smaller-scale fluctuations, especially localized MWs in the Lauder lidar, we believe that a reasonable approximation to the background temperature gradient can be inferred. Using SABER and the AMTM and lidar measurements, we infer an approximate mean
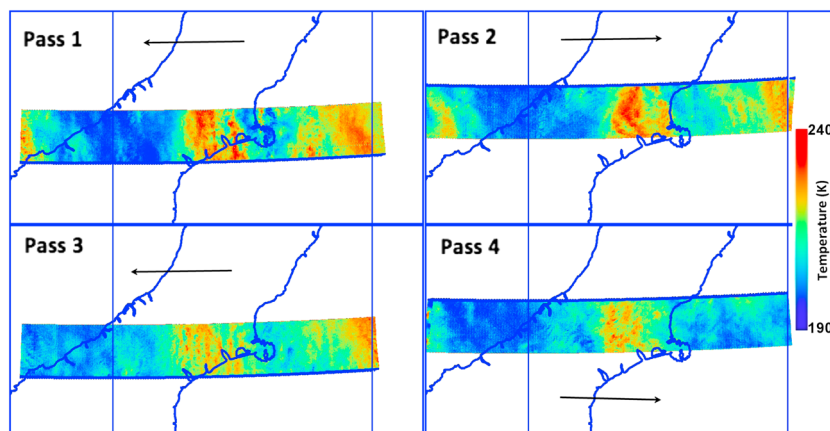

Figure 7. AMTM spatial keograms showing both the 240 km MW centered over New Zealand and several smaller-scale GWs.

Table 1. 240 km MW Temperature Perturbations and Corresponding MF Near 84 km

Pass Number	$\langle T' \rangle$ (K)	MF ($m^2 s^{-2}$)
1	8	6
2	7	5
3	6	3
4	8	6

temperature gradient from 80 to 87 km of ~2.5 K/km. This results in an estimate of the mean buoyancy frequency between ~80 km and 87 km of $N \sim 0.023 \, s^{-1}$ from equation (2).

The background wind was obtained using the Kingston radar. For the purposes of this analysis, we assume that the stationary MWs are largely observed toward the bottom side of the OH layer near 84 km, as these MWs are likely approaching a critical level near 90 km where the mean winds approach $0 \, ms^{-1}$. Furthermore, the sodium mixing ratios confirm that the amplitude of the ~240 km MW decreases rapidly above 85 km. For the smaller-scale waves, we assume that those with observable phase speeds toward the east (not MWs) are weighted toward the center of the OH layer as they are not approaching a critical level. For this reason, we assume the background wind at two different altitudes depending on the GW analysis, 87 km and 84 km, where the winds are ~ -25 and $-45 \, m \, s^{-1}$ respectively as shown in Figure 4.

4.3. Large-Scale MW Characterization and MF Estimation

The temperature perturbations for the ~240 km MW were found by subtracting the mean temperature for each flight segment. Smaller-scale perturbations were removed from the ~240 km GW using a smoothing spline fit to generate a low-pass characterization of the ~240 km MW and estimate the temperature perturbations associated with this MW. We assume that the temperatures measured by the AMTM are largely weighted toward the MW perturbations seen below ~85 km because of the expected strong phase averaging at higher altitudes. These temperature perturbations are likely an underestimate of the actual temperature perturbations between 80 and 85 km due to averaging within the OH layer. However, given our lack of information about the shape of the OH layer in the complex mixing environment accompanying breaking and dissipation at these altitudes, a correction factor may provide an inaccurate and potentially large overestimate of the temperature perturbation. The MF for the ~240 km MW for each pass was calculated using equation (3) and other parameters specified above. The ~240 km MW parameters and corresponding MFs calculated from the AMTM are summarized in Table 1. These varied from 3 to 6 $m^2 s^{-2}$ and are similar to the mean values at this altitude. As noted above, however, these values are likely a significant underestimate of the MF of the ~240 km MW where its amplitude is larger than the estimates from the AMTM in Table 1.

The sodium mixing ratios provide an alternate means of estimating temperature perturbations of the ~240 km MW at these altitudes. The mixing ratio yields a relative parcel displacement, and from this a temperature perturbation can be calculated. The displacements in mixing ratio contour from ~83 km for each pass are summarized in Table 2. Using an adiabatic lapse rate of 9.5 K/km and the background temperature gradient of ~2.5/km, a temperature perturbation estimation can be obtained, and these estimates are also given in Table 2. We use the winds near ~83 km, which are 55 $m \, s^{-1}$ toward the east, in order to calculate the MF here. The MF values are summarized in Table 2. These values are larger than mean MF values and range from 17 to 68 $m^2 s^{-2}$, which suggest strong variation in propagation conditions of the ~240 km MW on each pass. The difference in temperature measurements between the AMTM and sodium mixing ratio is due to the averaging associated with the AMTM and its likely small contribution from the lower altitudes where the ~240 km MW is large, given that the OH layer appears to be centered where we see little to no perturbations in the sodium mixing ratios.

Assessing uncertainties in GW MF estimates is important for defining mean values and their range of variability under various forcing and propagation conditions. Often, uncertainties in MF magnitudes are quite large due to imprecise estimates of GW amplitudes, intrinsic frequencies, and variable environments. This is especially the case in using airglow intensity measurements, where the relation between intensity and temperature perturbations may vary by a factor of up to ~10 [*Hickey and Yu*, 2005], causing MF uncertainties of up to ~100 times for slow GW phase speeds

Table 2. 240 km MW Mixing Ratio Vertical Displacements Near 83 km

Pass #	dz (km)	T' (K)	MF ($m^2 s^{-2}$)
1	2	24	68
2	1.5	18	38
3	1	12	17
4	1.5	18	38

Table 3. Estimated Upper Bound MF Values for the ~240 km MW Approximated From 83 to 87 km

Altitude (km)	$c - u$ (m s^{-1})	λ_z (km)	MF Limit (m^2 s^{-2})
83	55	15.2	96
84	45	12.4	52
87	25	6.8	9

and up to ~10 times for higher GW phase speeds. In particular, previous estimates using airglow brightness with claimed uncertainties of only approximately tens of percent cannot be legitimate in light of the *Hickey and Yu* [2005] analysis.

Direct estimates of T' provided by the new AMTMs largely overcome these extreme uncertainties. However, there remain significant uncertainties that could cause a traditional error analysis to imply that MFs remain almost entirely uncertain. To provide more justified bounds on MFs in such cases, we note that a well-constrained T' effectively defines a lower bound on MF in cases where measurements provide reasonable characterization of the GW intrinsic properties. Nevertheless, this always yields an underestimate, due to the phase averaging inherent in the AMTM T' estimate. Similarly, identification of GW parameters and their environments also enables an approximate upper limit imposed by a GW saturation condition, e.g., $u'_{max} \sim (c - u)$ [*Fritts*, 1984], for which there is observational, theoretical, and modeling evidence [see *Fritts and Alexander*, 2003].

In our case, MWs approaching a critical level at ~90 km imply that the peak MF will occur near where $u' = (c - u)$ and will decrease as the critical level is approached. The resulting MF estimates at 83, 84, and 87 km are summarized in Table 3. These suggest maximum MFs ranging from ~96 m^2 s^{-2} at 83 km to less than ~10 m^2 s^{-2} at 87 km. Our calculations above are within these bounds, and our data also agree with the strong dissipation that must be occurring as the MWs approach the critical level near 90 km.

Given the strong dissipation of this MW up to 85 km, and very weak influences above, we assume for further analysis that the ~240 km MW does not have large wind and temperature perturbations affecting the propagation environment of small-scale GWs observed at the altitude of the AMTM. However, it should be acknowledged that this MW most likely has an increasing influence on small-scale GW propagation at lower altitudes where its amplitude is large.

4.4. Small-Scale GW Characterization and MF Calculations

On each flight segment of the RF22 flight, there were smaller-scale dynamics observed over the South Island. Each of these occurred accompanying the central brighter, and warmer, phase of the ~240 km MW, suggesting strong influences of the ~240 km MW structure on the character and vertical propagation of these smaller-scale GWs and the potential influences of this ~240 km MW on the production of instabilities and secondary GWs. AMTM vertical views of these four events with the large-scale ~240 km MW background subtracted are shown in Figure 8. In each case, the smaller-scale dynamics were aligned principally in the zonal plane and their λ_h varied from ~25 to 28 km.

The dotted boxes in Figure 8 show the region of the image used for the calculation of T' and λ_h. To obtain T', we average the temperature meridionally as the observed GWs are aligned in the north-south direction. These averages use 10 pixels of the AMTM, so error due to AMTM noise is sufficiently reduced. The average difference between the temperature maxima and minima in the boxed areas was used to determine the approximate T'. In order to calculate a corresponding λ_h, a Lomb Scargle periodogram was used on the images in Figure 8. Our smaller-scale GW analysis is limited to the FOV of the AMTM. The images in Figure 8 are ~45 km meridionally by ~90 km zonally, and the smaller-scale GWs analyzed in this section have a $\lambda_h < 45$ km. The phase speed c for each observation was calculated by tracing phase movement across successive images in time and compensating for the speed of the GV. From these observed phase speeds, the intrinsic phase speed, $c_i = c - u$, for each event was calculated using the mean horizontal wind, u, estimated from the radar measurements. In order to account for expected uncertainties in the local mean wind, we also calculate the MF assuming that u is larger and smaller by 15 m s^{-1}. This allows for estimates of the possible range of MFs given the inherent uncertainties in the available horizontal wind information. Given the differing nature of the small-scale dynamics, each pass is described separately below.

4.4.1. Pass 1

This GW was observed to be propagating with a phase speed of ~100 m s^{-1} toward the east. The atmospheric conditions allow for this GW to propagate to higher altitudes, so we assume propagation through the entire OH layer. The measured T' is ~7 K, the horizontal wavelength is 28 km, and for a background wind of
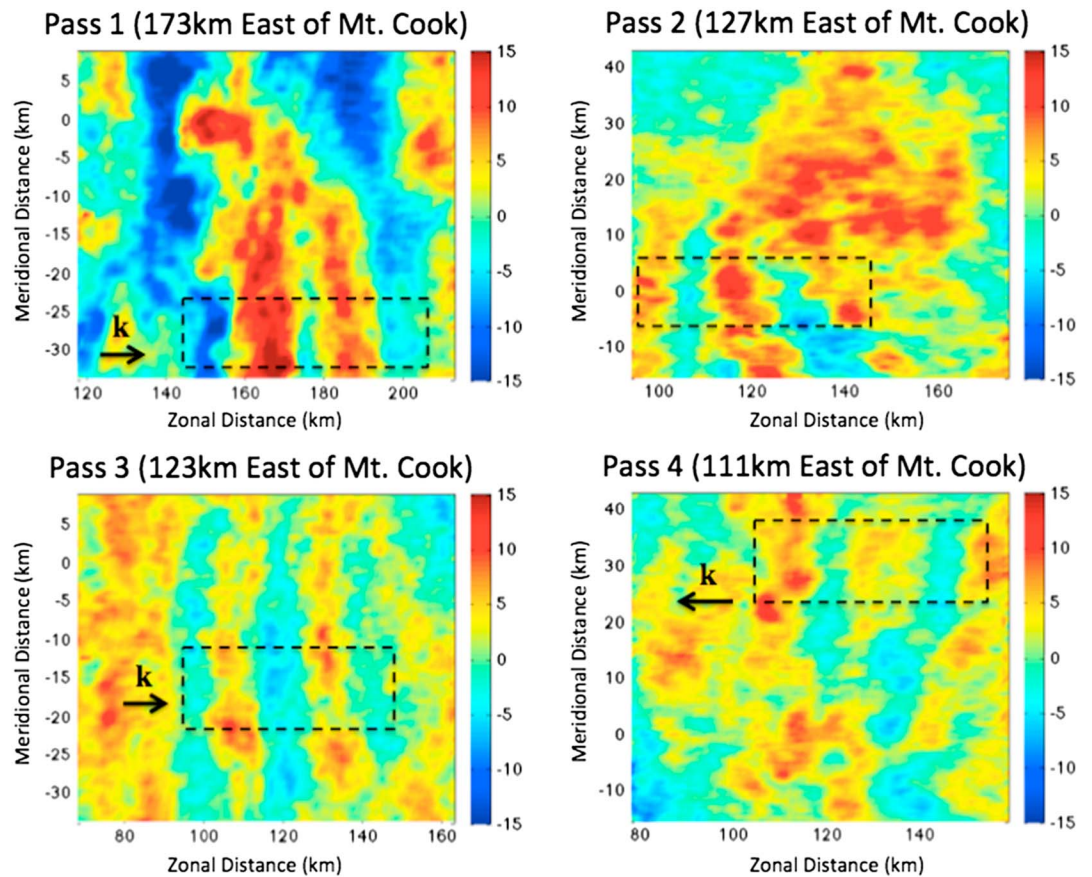
Figure 8. Overhead AMTM temperature maps of observed small-scale GWs during the four flight segments over Mount Cook, NZ. The dashed boxes show the areas used for calculating temperature perturbations and wavelength using a Lomb Scargle periodogram. The arrows denote the intrinsic direction of propagation of the observed GWs.

$-25\,\mathrm{m\,s^{-1}}$ at 87 km, the corresponding MF is $\sim 105\,\mathrm{m^2\,s^{-2}}$ which is ~ 10–20 times the mean at this altitude. The MF for zonal winds of $\pm 15\,\mathrm{m\,s^{-1}}$ about the mean wind assumed above also yielded vertical propagation in each case, with MF ranging from ~ 70 to $200\,\mathrm{m^2\,s^{-2}}$.

4.4.2. Pass 2

This feature appears to be largely confined to the FOV of the GV AMTM and is not seen in the side-viewing cameras, it evolves somewhat in shape over the intervals observed, and the relative motion ($\sim -24\,\mathrm{m\,s^{-1}}$) appears to be the same as the mean wind ($\sim -25\,\mathrm{m\,s^{-1}}$). Thus, we believe these features to be instabilities that simply advect with the mean wind at this altitude.

4.4.3. Pass 3

Similar to the first pass, this GW is propagating with an observed phase speed of $130\,\mathrm{m\,s^{-1}}$ to the east. At the central OH altitude of ~ 87 km, the measured phase speed implies that the observed GW is evanescent. However, given the significant $T' \sim 5$ K, it is likely that this GW is ducted at a nearby eastward wind or N^2 maximum at a lower altitude, given the wind profile implied by the meteor radar and the N^2 maximum implied by SABER from ~ 82 to 85 km. The stronger eastward winds measured by the meteor radar just a few kilometers below 87 km would allow this GW to be in a region of vertical propagation below the evanescent region near 87 km.

Table 4. Small-Scale Parameters for Passes 1–4 Obtained From Figure 7

Pass #	$<T'>$ (K)	c (m s^{-1})	u (m s^{-1})	c_i (m s^{-1})	λ_h (km)	m^2 (m^{-2})	λ_z (km)
1	7	−100	−25	−75	28	3.88E−08	31.9
2	6	−24	−25	--	28	--	--
3	5	−135	−25	−110	28	−1.23E−08	--
4	4.4	0	−45	45	25	1.96E−07	14.2

Table 5. Small-Scale GW MF Calculated Without Correcting for Integration Over the OH Layer for Passes 1 and 4

		MF ($m^2 s^{-2}$)		
Pass #	Altitude (km)	$u - 15$ ($m s^{-1}$)	u ($m s^{-1}$)	$u + 15$ ($m s^{-1}$)
1	87	68	105	212
4	84	33	21	13

4.4.4. Pass 4

The GW in this case has an observed phase speed near zero, suggesting a smaller-scale MW that is also approaching a critical level. It also appears to have small-scale structure suggesting that it may be exhibiting instability accompanying its decreasing vertical wavelength and amplitude. For this reason, we use 84 km as our analysis altitude, similar to that of the ~240 km MW. The measured $T' \sim 4.4$ K and horizontal wavelength of ~25 km implies a MF ~ 21 $m^2 s^{-2}$, thus with lower limits varying from 13 to 33 $m^2 s^{-2}$ due to an estimated uncertainty in the background wind of ± 15 $m s^{-1}$. While we have assumed that this is a MW because of the approximately zero phase speed and the small-scale structure at higher altitudes, we note the complex environment through which this GW must propagate to reach the MLT region. This GW was observed above a region of low stability and decreasing temperature as measured by both SABER and the Lauder lidar. This region is likely a layer in which MWs are breaking, and the observed GW from this pass could either be a MW contributing to the breaking dynamics and retaining a coherent structure but with smaller amplitude as observed in modeling of GW breaking [*Fritts et al.*, 2009] or this could be a secondary GW coincidentally having the same phase speed as the source MWs. Of these possibilities, the former seems far more likely, as we are aware of no observations or modeling studies suggesting secondary GWs exhibiting this behavior.

The characteristics of each observation are summarized in Table 4. The MF calculations for passes 1 and 4 are summarized in Table 5. The MF estimates for passes 1 and 4 are very conservative as the T' is not corrected for averaging over the OH layer, which would yield a larger implied T' in all cases. As noted previously, the MW breaking environment at the bottom side of the OH layer adds complexity that makes confident estimates of the true T' challenging. We also performed these MF estimates for u increased and decreased by 15 $m s^{-1}$ relative to the estimated u in each case. The MF values computed for changes in u (and c_i) by 15 $m s^{-1}$ approximate the extrema of the possible MF values, given the uncertainties of the local horizontal wind u and phase speed c determinations from the AMTM. Nevertheless, we believe the central values to be more likely and so will use these as our best conservative estimates for these events.

5. Discussion

The MFs listed in Tables 1, 2, and 5 span a wide range of magnitudes for various observed GW scales and amplitudes. The ~240 km MW was estimated to have MFs ranging from 3 to 6 $m^2 s^{-2}$ at ~87 km by the AMTM and potentially MFs as large as 68 $m^2 s^{-2}$ from the sodium mixing ratio displacement estimates at a lower altitude where the MW amplitude is obviously much larger. This larger value is ~10 times larger than the mean values at this altitude, and this MF spans a region extending hundreds of kilometers zonally and meridionally. In comparison, the smaller-scale GWs observed in localized regions over South Island on flight segments 1 and 4 had large MFs with conservative estimates for pass 4 of ~20 $m^2 s^{-2}$ and conservative estimates for pass 1 of ~100 $m^2 s^{-2}$. Regardless of errors associated with these estimates, they may greatly underestimate the actual MF values depending on phase averaging of the small-scale GWs over the OH layer. Compared to the ~240 km MW, the smaller-scale GWs that were propagating had much larger MFs, and these range from as much as ~2–20 times typical mean magnitudes of ~5–10 $m^2 s^{-2}$ expected at these altitudes. While we note that these calculations may have large errors associated with them, even very conservative estimates show that the MF associated with the small-scale GWs is significant. These estimates demonstrate the potentially important role of such small-scale GWs in the overall momentum budget of the mesosphere and lower thermosphere.

The small-scale GWs examined here are also of interest because of the multiscale character of the environments that appeared to control where they achieved large amplitudes and MFs. During the first and third flight segments, the GWs were observed to have eastward intrinsic phase speeds. However, the observed small-scale GW on the third flight segment was evanescent, suggesting that this GW seen in the OH layer was likely ducted at a nearby layer, given its large OH layer amplitude. Observations on the fourth flight segment revealed a GW with an intrinsic phase speed toward the west and an observed phase speed of zero,

which was possibly a smaller-scale MW or other GW approaching a critical level. Thus, all of these GWs had apparently very different character, despite somewhat similar large-scale environments.

The different character of the three small-scale GWs discussed above suggests potentially different sources for these various GWs and/or different multiscale influences on their propagation into the MLT. One obvious potential source is the same South Island orography that generated the ~240 km MW that provided the background environment at higher altitudes. This could only be true for the small-scale GWs having $c \sim 0$ and $c_i > 0$. But this is the case for the small-scale GW on flight segment 4, which has an observed $c \sim 0$. The other small-scale GWs must have different initial c and c_i (and sources) given their large negative c and especially the $c_i < 0$ for flight segments 1 and 3.

Finally, as noted above, the small-scale GWs analyzed for the flight segments all occurred in the warm phase of the ~240 km MW, implying a significant influence of the ~240 km MW on the small-scale GW propagation and refraction with altitude. These cases are very similar to that observed at ALOMAR in northern Norway and analyzed by *Fritts et al.* [2014]. In that case, the larger GW scales within the multiscale GW field were found to strongly modulate the smaller-scale GW occurrence and amplitude, also leading to a very large momentum flux estimate. Thus, our observations of similar dynamics during DEEPWAVE appear to be further evidence of the importance of such multiscale dynamics that likely play major roles in the composition of the GW spectrum with altitude and the determination of the GWs that contribute most to momentum fluxes in the MLT.

6. Conclusions

The measurements described here occurred during the DEEPWAVE airborne measurement campaign that was performed in June and July 2014 over and around New Zealand. DEEPWAVE specifically targeted deep responses to orographic and nonorographic GW sources at lower altitudes extending to ~100 km.

GV airborne observations during DEEPWAVE Research Flight 22 on 13 July revealed a larger-scale, $\lambda_h \sim 240$ km MW extending ~600 km or more zonally and ~900 km or more meridionally. This large-scale MW yielded estimated MFs of ~ 3–$6\,m^2\,s^{-2}$ from AMTM altitudes and MFs of 17–$68\,m^2\,s^{-2}$ at altitudes near ~83 km in the sodium mixing ratios. Observations of localized smaller-scale GWs within the ~240 km MW field had $\lambda_h \sim 25$–28 km and yielded MF estimates ranging from $\sim 20\,m^2\,s^{-2}$ to $105\,m^2\,s^{-2}$ that are larger, and in some cases significantly larger, than mean values in the MLT. These results demonstrate the potentially significant impacts that small horizontal-scale GWs with large λ_z can have at higher altitudes. They also emphasize the likely importance of such multiscale GW dynamics and their influences on smaller-scale GW propagation and momentum fluxes in the MLT and potentially at lower altitudes. Indeed, such multiscale dynamics may be relatively common throughout the atmosphere and suggest the value of additional efforts to quantify these dynamics and effects with further quantitative observations and parallel numerical modeling.

References

Baker, D. B., and A. T. Stair (1988), Rocket measurements of the altitude distributions of the hydroxyl airglow, *Phys. Scr.*, *37*, 611–622.

Bossert, K., D. C. Fritts, P.-D. Pautet, M. J. Taylor, B. P. Williams, and W. R. Pendelton (2014), Investigation of a mesospheric gravity wave ducting event using coordinated sodium lidar and Mesospheric Temperature Mapper measurements at ALOMAR, Norway (69°N), *J. Geophys. Res. Atmos.*, *119*, 9765–9778, doi:10.1002/2014JD021460.

Cai, X., T. Yuan, Y. Zhao, P.-D. Pautet, M. J. Taylor, and W. R. Pendelton Jr. (2014), A coordinated investigation of the gravity wave breaking and the associated dynamical instability by Na lidar and Advanced Mesospheric Temperature Mapper over Logan, UT (41.7°N, 111.8°W), *J. Geophys. Res. Space Physics*, *119*, 6852–6864, doi:10.1002/2014JA020131.

Collins, R. L., and R. W. Smith (2004), Evidence of damping and overturning of gravity waves in the Arctic mesosphere: Na lidar and OH temperature observations, *J. Atmos. Sol. Terr. Phys.*, *66*, 867–879.

Collins, R. L., X. Tao, and C. S. Gardener (1996), Gravity wave activity in the upper mesosphere over Urbana, Illinois: Lidar observations and analysis of gravity wave propagation models, *J. Atmos. Sol. Terr. Phys.*, *58*(16), 1905–1926.

Eckermann, S. D. (1997), Influence of wave propagation on the Doppler spreading of atmospheric gravity waves, *J. Atmos. Sci.*, *54*, 2554–2573.

Ejiri, M. K., M. J. Taylor, T. Nakamura, and S. J. Franke (2009), Critical level interaction of a gravity wave with background winds driven by a large-scale wave perturbation, *J. Geophys. Res.*, *114*, D18117, doi:10.1029/2008JD011381.

Ern, M., P. Preusse, J. C. Gille, C. L. Hepplewhite, M. G. Mlynczak, J. M. Russell III, and M. Riese (2011), Implications for atmospheric dynamics derived from global observations of gravity wave momentum flux in stratosphere and mesosphere, *J. Geophys. Res.*, *116*, D19107, doi:10.1029/2011JD015821.

Espy, P. J., G. O. L. Jones, G. R. Swenson, J. Tang, and M. J. Taylor (2004), Seasonal variations of the gravity wave momentum flux in the Antarctic mesosphere and lower thermosphere, *J. Geophys. Res.*, *109*, D23109, doi:10.1029/2003JD004446.

Fritts, D. C. (1984), Gravity wave saturation in the middle atmosphere: A review of theory and observations, *Rev. Geophys.*, *22*, 275–308, doi:10.1029/RG022i003p00275.

Fritts, D. C., and M. J. Alexander (2003), Gravity wave dynamics and effects in the middle atmosphere, *Rev. Geophys.*, *41*(1), 1003, doi:10.1029/2001RG000106.

Fritts, D. C., and R. A. Vincent (1987), Mesospheric momentum flux studies at Adelaide, Australia: Observations and a gravity wave/tidal interaction model, *J. Atmos. Sci.*, *44*, 605–619.

Fritts, D. C., S. A. Vadas, and Y. Yamada (2002), An estimate of strong local gravity wave body forcing based on OH airglow and meteor radar observations, *Geophys. Res. Lett.*, *29*(10), 1429, doi:10.1029/2001GL013753.

Fritts, D. C., L. Wang, J. Werne, T. Lund, and K. Wang (2009), Gravity wave instability dynamics at high Reynolds numbers. Part 1: Wave field evolution at large amplitudes and high frequencies, *J. Atmos. Sci.*, *66*, 1126–1148.

Fritts, D. C., D. Janches, and W. K. Hocking (2010), Southern Argentina Agile Meteor Radar: Initial assessment of gravity wave momentum fluxes, *J. Geophys. Res.*, *115*, D19123, doi:10.1029/2010JD013891.

Fritts, D. C., D. Janches, H. Iimura, W. K. Hocking, J. V. Bageston, and N. M. P. Leme (2012), Drake Antarctic Agile Meteor Radar first results: Configuration and comparison of mean and tidal wind and gravity wave momentum flux measurements with Southern Argentina Agile Meteor Radar, *J. Geophys. Res.*, *117*, D02105, doi:10.1029/2011JD016651.

Fritts, D. C., P.-D. Pautet, K. Bossert, M. J. Taylor, B. P. Williams, H. Iimura, T. Yuan, N. J. Mitchell, and G. Stober (2014), Quantifying gravity wave momentum fluxes with Mesosphere Temperature Mappers and correlative instrumentation, *J. Geophys. Res. Atmos.*, *119*, 13,583–13,603, doi:10.1002/2014JD022150.

Fritts, D. C., et al. (2015), The Deep Propagating Gravity Wave Experiment (DEEPWAVE): An Airborne and Ground-Based Exploration of Gravity Wave Propagation and Effects from their Sources throughout the Lower and Middle Atmosphere, *Bull. Am. Meteorol. Soc.*, doi:10.1175/BAMS-D-14-00269.1.

Garcia, R. R., and S. Solomon (1985), The effect of breaking gravity waves on the dynamics and chemical composition of the mesosphere and lower thermosphere, *J. Geophys. Res.*, *90*, 3850–3868, doi:10.1029/JD090iD02p03850.

Haynes, P. H., C. J. Marks, M. E. McIntyre, T. G. Shephard, and K. P. Shine (1991), On the "downward control" of extratropical diabatic circulations by eddy-induced mean zonal forces, *J. Atmos. Sci.*, *48*(657–678), 1991.

Hecht, J. H., R. L. Walterscheid, D. C. Fritts, J. R. Isler, D. C. Senft, C. S. Gardner, and S. J. Franke (1997), Wave breaking signatures in OH airglow and sodium densities and temperatures: 1. Airglow imaging, Na lidar, and MF radar observations, *J. Geophys. Res.*, *102*(D6), 6655–6668, doi:10.1029/96JD02619.

Hertzog, A., M. J. Alexander, and R. Plougonven (2012), On the intermittency of gravity wave momentum flux in the stratosphere, *J. Atmos. Sci.*, *69*, 3433–3448.

Hickey, M. P., and Y. Yu (2005), A full-wave investigation of the use of a "cancellation factor" in gravity wave-OH airglow interaction studies, *J. Geophys. Res.*, *110*, A01301, doi:10.1029/2003JA01372.

Hitchman, M., K. W. Bywaters, D. C. Fritts, L. Coy, E. Kudeki, and F. Surucu (1992), Mean winds and momentum fluxes over Jicamarca, Peru, during June and August 1987, *J. Atmos. Sci.*, *49*, 2372–2383.

Holdsworth, D. A., I. M. Reid, and M. A. Cervera (2004), Buckland Park all-sky interferometric meteor radar, *Radio Sci.*, *39*, RS5009, doi:10.1029/2003RS003014.

Holton, J. R. (1982), The role of gravity wave induced grad and diffusion in the momentum budget of the mesosphere, *J. Atmos. Sci.*, *39*, 791–799.

Holton, J. R. (1984), The generation of mesospheric planetary waves by zonally asymmetric gravity wave breaking, *J. Atmos. Sci.*, *41*, 3427–3430.

Kim, Y.-J., S. D. Eckermann, and H.-Y. Chun (2003), A overview of the past, present and future of gravity-wave drag parameterization for numerical climate and weather prediction models, *Atmos. Ocean*, *41*, 65–98.

Lieberman, R. S., et al. (2000), Comparison of mesospheric and lower thermospheric residual wind with High Resolution Doppler Imager, medium frequency and meteor radar winds, *J. Geophys. Res.*, *105*(D22), 27,023–27,035, doi:10.1029/2000JD900363.

Lieberman, R. S., D. A. Ortland, D. M. Riggin, Q. Wu, and C. Jacobi (2010), Momentum budget of the migrating diurnal tide in the mesosphere and lower thermosphere, *J. Geophys. Res.*, *115*, D20105, doi:10.1029/2009JD013684.

Lieberman, R. S., D. M. Riggin, and D. E. Siskind (2013), Stationary waves in the wintertime mesosphere: Evidence for gravity wave filtering by stratospheric planetary waves, *J. Geophys. Res. Atmos.*, *118*, 3139–3149, doi:10.1002/jgrd.50319.

Murphy, D. J., and R. A. Vincent (1993), Estimates of momentum flux in the mesosphere and lower thermosphere over Adelaide, Australia, from March 1985 to February 1986, *J. Geophys. Res.*, *98*(D10), 18,617–18,638, doi:10.1029/93JD01861.

Nakamura, T., T. Tsuda, M. Yamamoto, S. Fukao, and S. Kato (1993), Characteristics of gravity waves in the mesosphere observed with the middle and upper atmosphere radar: 1. Momentum flux, *J. Geophys. Res.*, *98*(D5), 8899–8910, doi:10.1029/92JD02978.

Namboothiri, S. P., T. Tsuda, M. Tsutsumi, and T. Nakamura (1996), Simultaneous observations of mesospheric gravity waves with the MU radar and a sodium lidar, *J. Geophys. Res.*, *101*(D2), 4057–4063, doi:10.1029/95JD03299.

Nastrom, G. D., and D. C. Fritts (1992), Sources of mesoscale variability of gravity waves. I: Topographic excitation, *J. Atmos. Sci.*, *49*, 101–110.

Nielsen, K., M. J. Taylor, R. E. Hibbins, M. J. Jarvis, and J. M. Russell III (2012), On the nature of short-period mesospheric gravity wave propagation over Halley, Antarctica, *J. Geophys. Res.*, *117*, D05124, doi:10.1029/2011JD016261.

Pautet, P.-D., M. J. Taylor, W. R. Pendelton Jr., Y. Zhao, T. Yuan, R. Esplin, and D. McLain (2014), An Advanced Mesospheric Temperature Mapper for high-latitude airglow studies, *Appl. Optics*, *53*(26), 5934–5943.

Pfister, L., S. Scott, M. Loewenstein, S. Bowen, and M. Legg (1993), Mesoscale disturbances in the tropical stratosphere excited by convection: Observations and effects on the stratospheric momentum budget, *J. Atmos. Sci.*, *50*, 1058–1075.

Reid, I. M., R. Ruster, P. Czechowsky, and G. Schmidt (1988), VHF radar measurements of momentum flux in the summer polar mesosphere over Andenes (69°N, 16°E), Norway, *Geophys. Res. Lett.*, *15*(11), 1263–1266, doi:10.1029/GL015i011p01263.

Remsberg, E. E., et al. (2008), Assessment of the quality of the version 1.07 temperature-versus-pressure profiles of the middle atmosphere from TIMED/SABER, *J. Geophys. Res.*, *113*, D17101, doi:10.1029/2008JD010013.

She, C. Y., and R. P. Lowe (1998), Seasonal temperature variations in the mesopause region at mid-latitude: Comparison of lidar and hydroxyl rotational temperatures using WINDII/UARS OH height profiles, *J. Atmos. Sol. Terr. Phys.*, *60*, 1573–1583.

Simkhada, J. B., M. J. T. Snively, and S. J. Franke (2009), Analysis and modeling of ducted and evanescent gravity waves observed in the Hawaiian airglow, *Ann. Geophys.*, *27*, 3213–3224.

Smith, A. K. (2003), The origin of stationary planetary waves in the mesosphere, *J. Atmos. Sci.*, *60*, 3033–3041.

Taylor, M. J., W. R. Pendleton, S. Clark, H. Takahashi, D. Gobbi, and R. A. Goldberg (1997), Image measurements of short-period gravity waves at equatorial latitudes, *J. Geophys. Res.*, *102*(D22), 26,283–26,299, doi:10.1029/96JD03515.

Tsuda, T., Y. Murayama, M. Yamamoto, S. Kato, and S. Fukao (1990), Seasonal variation of momentum flux in the mesosphere observed with the MU radar, *Geophys. Res. Lett.*, *17*(6), 725–728, doi:10.1029/GL017i006p00725.

Vincent, R. A., and I. M. Reid (1983), HF Doppler measurements of mesospheric momentum fluxes, *J. Atmos. Sci.*, *40*, 1321–1333.

Wang, D.-Y., and D. C. Fritts (1990), Mesospheric momentum fluxes observed by the MST radar at Poker Flat, Alaska, *J. Atmos. Sci.*, *47*, 1512–1521.

Williams, B. P., D. C. Fritts, C. Y. She, and R. A. Goldberg (2006), Gravity wave propagation through a large semidiurnal tide and instabilities in the mesosphere and lower thermosphere during the winter 2003 MaCWAVE rocket campaign, *Ann. Geophys.*, *24*, 1199–1208.

Wilson, R., M. L. Chanin, and A. Hauchecorne (1991), Gravity waves in the middle atmosphere observed by Rayleigh lidar: 2. Climatology, *J. Geophys. Res.*, *96*(D3), 5169–5183, doi:10.1029/90JD02610.

Yuan, T., P.-D. Pautet, Y. Zhao, X. Cai, N. R. Criddle, M. J. Taylor, and W. R. Pendleton Jr. (2014), Coordinated investigation of midlatitude upper mesospheric temperature inversion layers and the associated gravity wave forcing by Na lidar and Advanced Mesospheric Temperature Mapper in Logan, Utah, *J. Geophys. Res. Atmos.*, *119*, 3756–3769, doi:10.1002/2013JD020586.

Yue, J., S. L. Vadas, C.-Y. She, T. Nakamura, S. C. Reising, H.-L. Liu, P. Stamus, D. A. Krueger, W. Lyons, and T. Li (2009), Concentric gravity waves in the mesosphere generated by deep convective plumes in the lower atmosphere near Fort Collins, Colorado, *J. Geophys. Res.*, *114*, D06104, doi:10.1029/2008JD011244.